Research in Astronomy and Astrophysics, 25:035014 (13pp), 2025 March

https://doi.org/10.1088/1674-4527/adb938
CSTR: 32081.14.RAA.adb938

Comparison of Simulated Backgrounds with In-orbit Observations for HXI Onboard ASO-S

Hao-Xiang Wang[1,2], Zhe Zhang[1,2], Wei Liu[1,2], Xian-Kai Jiang[1,2], Deng-Yi Chen[1,2], Yi-Ming Hu[1,2], and Yang Su[1,2]
[1] Key Laboratory of Dark Matter and Space Astronomy, Purple Mountain Observatory, Chinese Academy of Sciences, Nanjing 210023, China; zhangzhe@pmo.ac.cn
[2] School of Astronomy and Space Science, University of Science and Technology of China, Hefei 230026, China
Received 2024 September 23; revised 2025 January 18; accepted 2025 February 17; published 2025 March 18

Abstract

The Hard X-ray Imager (HXI) payload, a component of China's Advanced Space-based Solar Observatory satellite, is designed to observe solar X-ray emissions in the 30–200 keV range, with the aim of investigating non-thermal physical processes during solar flares. Before launch, Geant4 simulations were employed to assess the on-orbit background of the HXI instrument, evaluating its performance and potential to achieve its scientific objectives. This study addresses issues identified in previous simulations and conducts further analyses to examine the distribution of background counts across the 99 detectors. The results demonstrate alignment between simulations and observations at low and medium geomagnetic latitudes; however, challenges persist at high geomagnetic latitudes due to limitations in the current albedo photon model. This investigation provides insights into background sources from various particles, enhances understanding of space background characteristics, and offers guidance for background subtraction in imaging processes.

Key words: instrumentation: detectors – Sun: X-rays, gamma-rays – (cosmology:) cosmic background radiation – gamma-rays: diffuse background

1. Introduction

The Advanced Space-based Solar Observatory (ASO-S), also known as Kuafu-1 in China, was successfully launched from the Jiuquan Satellite Launch Center on 2022 October 8, at 23:43 UT, aboard a Long March 2D launch vehicle. ASO-S is China's first comprehensive dedicated solar observatory in space, with the primary objective of observing solar magnetic fields, solar flares, and coronal mass ejections (CMEs). To accomplish this mission, ASO-S is equipped with three main payloads: the Full-disk MagnetoGraph (FMG), the Lyα Solar Telescope (LST), and the Hard X-ray Imager (HXI). The FMG is designed to image the solar photospheric vector magnetic field, the LST to observe CMEs, and the HXI to image solar flares. These instruments work in concert to provide simultaneous observations of the full Sun's vector magnetic field, high-energy imaging spectroscopy of solar flares, and the formation and evolution of solar flares and CMEs on the solar disk and inner corona (Gan et al. 2019).

Satellite-borne detectors are exposed to intense space radiation, including cosmic rays, diffuse X-rays, solar flares, Earth albedo, and trapped charged particles in radiation belts. This radiation not only damages sensitive detectors but also generates background signals during scientific observations of target sources. These background signals can interfere with target source signals, compromising observational accuracy. In extreme cases, background signals may completely obscure target source signals, impeding normal observations. Space backgrounds are instrument-specific and depend on detector type and orbital parameters (e.g., Rothschild et al. 1998; Jahoda et al. 2006; Tawa et al. 2008; Fukazawa et al. 2009). Pre-launch estimation of in-orbit background for each space instrument is crucial for optimizing instrument design and assessing its capacity to achieve scientific objectives. GEometry ANd Tracking (Geant4, Agostinelli et al. 2003; Allison et al. 2006, 2016), a versatile toolkit for simulating particle-matter interactions, is widely used in nuclear and accelerator physics, as well as medical and space sciences. It has become a preferred tool for predicting in-orbit backgrounds of space instruments (e.g., Tenzer et al. 2010; Campana et al. 2013; Xie & Pearce 2018; Xiao et al. 2023). The accuracy of these simulations can be verified through post-launch in-orbit observations, validating both simulation methods and assumed models. For instance, Mizuno et al. (2004) verified the cosmic ray background flux model using data from the GLAST balloon flight experiment.

Before the satellite launch, simulations of the HXI background were conducted (Liu et al. 2022). While the simulation results generally align with the actual background observed in orbit, some discrepancies are evident. Notably, the distribution of counts among the detectors in the in-orbit data exhibits significant variations, indicating differing background counts across detectors at various positions. This discrepancy was not accounted for in previous simulations. Consequently, it is necessary to enhance the HXI background simulation to

improve the alignment between simulation results and in-orbit data. This enhancement will facilitate a more thorough investigation of HXI's background, provide more reliable background data for scientific observations, and offer valuable insights for background subtraction.

The structure of this paper is as follows: Section 2 briefly introduces the mass models of the ASO-S, with particular emphasis on the HXI. Section 3 presents an analysis of background and compares simulation results with observational data. Finally, Section 4 summarizes the findings.

2. Mass Modeling

The ASO-S mass model was constructed under the framework of Geant4 Version 11.00.p02. It comprises three key components: detector constructions, primary particles, and physics processes, which are detailed below.

2.1. Detector Construction

The ASO-S is equipped with three payloads: LST, FMG, and HXI. This study focuses on the HXI, designed to observe solar X-rays within the 30–200 keV energy range. The HXI's primary objective is to collect data on the spatial and energy distributions of solar X-ray sources, enabling imaging capabilities (Zhang et al. 2019). To achieve X-ray imaging, the HXI employs a spatially modulated Fourier-transformation technique similar to that used by the YOHKOH/HXT instrument (Kosugi et al. 1991). The HXI system comprises three main components: a collimator, a spectrometer, and an electrical control box. The collimator consists of front and back parallel grid plates, with the front plate directly facing the Sun. This plate features grid pairs with varying pitches and placement angles, creating 91 sub-collimator sets for X-ray modulation. These sub-collimators capture data on the spatial distribution of incoming photons, which, in conjunction with the spectrometer, facilitate X-ray imaging. The HXI's field of view (FOV) is approximately $40\farcm3$, determined by the dimensions of the front and rear grids. The spectrometer, positioned behind the collimator, consists of a lanthanum bromide ($LaBr_3$) scintillator detector that measures the energy of photons modulated by the collimator. The $LaBr_3$ crystals, doped with 0.5% cerium, measure 25 mm in both diameter and length. The mass model of the HXI was shown in Figure 1. Table 1 elucidates the orbital parameters of ASO-S, complemented by the performance indices of HXI.

To obtain more reliable results, it is crucial to construct a comprehensive satellite mass model and accurately represent the energy spectrum and angular distribution of space particles. The spectral and angular distribution details of particles from various sources are input into Geant4 for analysis, which subsequently yields the background information.

As noted by Liu et al. (2022), we utilized CADMesh (Poole et al. 2012) in conjunction with manual methods to construct

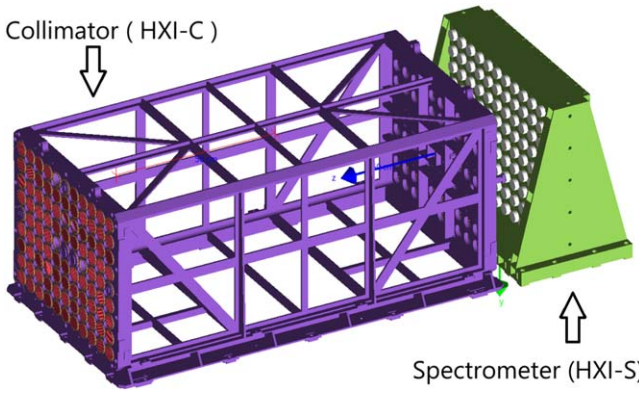

Figure 1. The mass model of the HXI, generated by Geant4 visualization.

Table 1
Orbital Parameters of ASO-S and Performance of HXI

	Parameter	Value
ASO-S	Orbit Altitude	720 km
	Orbit Inclination Angle	$98\fdg275$
	Descending Node	6:00 AM
HXI	Range of Energy	~15–300 keV
	FOV	$\sim40\farcm3$
	Energy Resolution (FWHM)	~16.6% @ 32 keV
	Temporal Resolution	regular mode: 4 s burst mode: configurable from 0.125 to 2 s
	Dead Time	2 μs
	Spatial Resolution	$\sim3\farcs1$
	Pointing Accuracy (SAS)	$<0\farcs2$

the mass model for ASO-S. Based on the previous model, we refined the grating arrangement to align with actual conditions, added blind gratings (2 mm thick tungsten plates) in front of the background detectors, and corrected material and structural errors from the previous model. Furthermore, we incorporated multiple layers of thermal insulation materials for the satellite's orbital thermal management, into the simulation model, approximated by 0.25 mm thick aluminum. Figure 2 depicts the final mass model of the complete satellite.

2.2. Background Models

The space environment surrounding Earth contains diverse particles, making it impractical to account for all of them. Previous simulations indicate that primary charged particles, cosmic diffuse X-rays (CXB), and albedo photons contribute predominantly to the in-orbit backgrounds of HXI outside the radiation belt (for more details on each component, refer to Liu et al. 2022).

The inner radiation belt, located at altitudes ranging from approximately 600 to 10,000 km above the Earth's surface, is

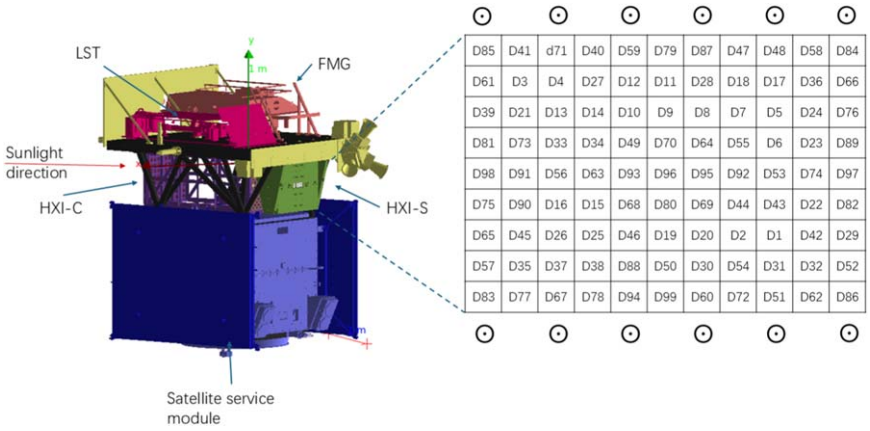

Figure 2. The left side of the image shows the mass model of ASO-S in Geant4. Adiabatic material wrapped around the satellite is not displayed in order to show the internal structure; while the right side displays the layouts of all HXI detector units (toward the Sun).

predominantly composed of high-energy protons and electrons. The offset between the Earth's magnetic dipole axis and its rotational axis, combined with the geomagnetic field's influence, creates a region near the South Atlantic where the magnetic field strength is significantly weaker. As a result, high-energy charged particles from the radiation belt can more readily penetrate into lower Earth orbits, with some reaching altitudes as low as 200 km. This region is referred to as the South Atlantic Anomaly (SAA). Due to the high and highly variable background radiation in the outer radiation belt, observational data from this region are unreliable. Therefore, this study will exclude the outer radiation belt from its scope.

Key parameters used in calculating multiple components are as follows:

(1) *Zenith angle*. The angle between the zenith and the top of the atmosphere (H_A = 40 km from sea level) at the satellite altitude. It determines the distribution of particles from different sources, with primary particles being shielded by the Earth, while secondary particles originate from the direction of the Earth. For the ASO-S, zenith angle $\theta \approx 116°$ (Liu et al. 2022).

As seen in Figure 3, the zenith angle is θ when the satellite is at point O. Due to the Earth's shielding effect, primary particles cannot reach the satellite in the white region (Area II); thus, the primary particle flux from this region is assumed to be zero. In contrast, the angular distribution of primary particles in the light pink region (Area I) is considered uniform.

(2) *Geomagnetic latitude θ_M and average geomagnetic cutoff R_{cutoff} (in GV)*. Primary charged particles are modulated by Earth's magnetic field upon entering low Earth orbit. Secondary particles, predominantly produced by the interaction of primary charged particles with the atmosphere, are also influenced by the geomagnetic field. Geomagnetic latitude is typically used to describe the distribution of Earth's magnetic field. The energy spectra at different geomagnetic latitudes are described by the corresponding geomagnetic cutoff rigidity. It can be described as (Zombeck 2006)

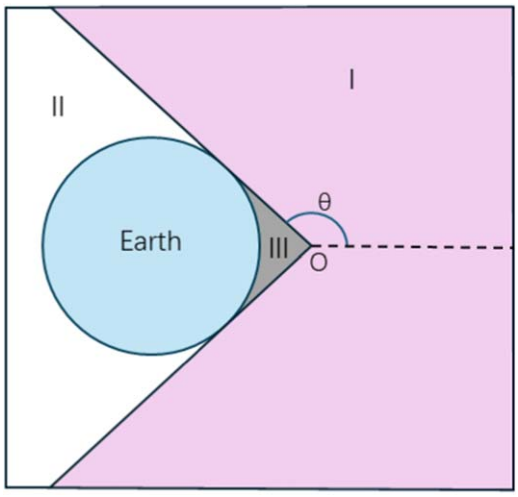

Figure 3. The impact of the Earth's shielding effect on the angular distribution of particles.

$$R_{\text{cutoff}} = 14.9 \times \left(1 + \frac{h}{R_{\oplus}}\right)^{-2} \times \cos^4 \theta_M \quad (1)$$

The altitude of the satellite is $h = 720$ km, and $R_{\oplus}$ represents the radius of the Earth, which is 6374 km. The symbol θ_M denotes the geomagnetic latitude. Figure 4 illustrates the change in R_{cutoff} concerning the geomagnetic latitude.

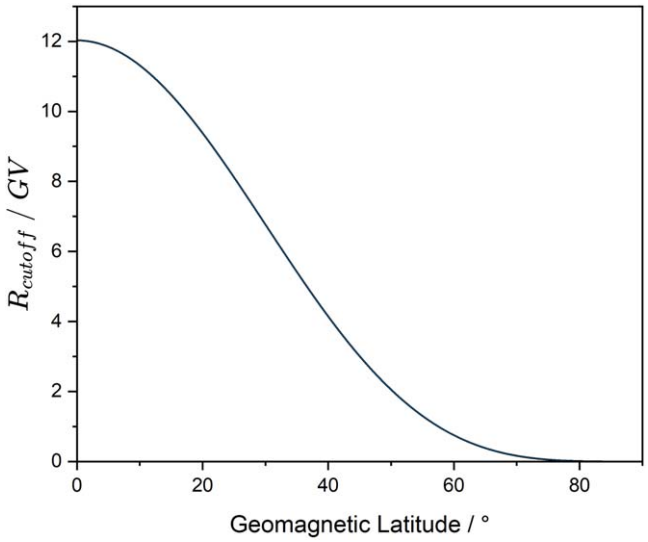

Figure 4. Variation of the average geomagnetic cutoff rigidity $R_{\rm cutoff}$ with geomagnetic latitude at an altitude of 720 km.

(3) Solar modulation: The value of solar modulation ϕ ranges from approximately 500 MV for solar activity minimum to approximately 1100 MV for solar activity maximum (Mizuno et al. 2004). The Sun is expected to peak in its current activity cycle by 2024. For this simulation, we have chosen to set ϕ at 1100 MV, a common value for solar activity at its peak.

The spectrum of background particles is primarily influenced by orbital altitude, inclination, and solar activity level. By considering the satellite's orbital characteristics, we can determine the spectrum of background particles originating from various sources.

2.2.1. Primary Charged Particles

Primary charged particles originate from outer space, predominantly composed of protons and α particles, alongside minor quantities of electrons.

The energy spectrum of primary charged particles can be described by a power-law distribution with modulation parameters (Mizuno et al. 2004).

$$F = A\left[\frac{R(E_k)}{GV}\right]^{-a} \times \frac{(E_k + Mc^2)^2 - M^2c^4}{(E_k + Mc^2 + Ze\phi)^2 - M^2c^4} \times \frac{1}{1 - (R/R_{\rm cutoff})^{-r}} \quad (2)$$

The equation includes the rigidity R, kinetic energy E_k of the particles, the magnitude of the electron charge e, the atomic number of the particles Z, the particle mass M, the speed of light c, and the solar modulation parameter ϕ.

The parameters for various primary charged particles can be derived by fitting experimental data obtained from the Alpha Magnetic Spectrometer (AMS) (Alcaraz et al. 2000a, 2000b, 2000c), as shown in Table 2.

Table 2
Parameters of Different Primary Charged Particles in Equation (2)

Particle	Parameter				
	$A/s^{-1}\ m^{-2}\ sr^{-1}\ MeV^{-1}$	a	Z	Mc^2/GeV	r
proton	23.9	2.83	1	0.938	12
alpha	1.5	2.77	2	3.726	12
electron	0.65	3.3	1	0.511×10^{-3}	6

The flux of low-energy primary cosmic rays in ASO-S orbits is significantly attenuated due to geomagnetic modulation. Although primary particles with energies exceeding hundreds of GeV are not impeded by the geomagnetic field, their initial fluxes are inherently low. Moreover, the simulation's efficacy diminishes for high-energy particles. Consequently, the simulation considers only charged particles within the 10 MeV to 200 GeV energy range.

2.2.2. Cosmic X-Rays Background (CXB)

CXB refers to cosmic X-rays originating primarily from black holes and neutron stars located in the Milky Way's core (Churazov et al. 2007). The energy spectrum of CXB is widely accepted to be isotropic and consistent across various near-Earth locations, simplifying its analysis. Numerous satellites have contributed to gathering CXB spectral data, as evidenced by studies from Gendreau et al. (1995), Watanabe et al. (1999), Churazov et al. (2007), and Ajello et al. (2008). The CXB spectrum up to 890 keV can be accurately represented by a double power-law (PL) fit. For energies above 890 keV, we utilize the Fermi Large Area Telescope (LAT) results (Atwood et al. 2009) and extrapolate to lower energies from E > 100 MeV.

$$\frac{dI(E)}{dE}(\text{photons cm}^{-2}\ \text{s}^{-1}\ \text{sr}^{-1}\ \text{keV}^{-1}) = \begin{cases} \dfrac{C}{(E/E_b)^{\alpha_1} + (E/E_b)^{\alpha_2}}, & E \leqslant 890\ \text{keV} \\ 0.95 \times 10^{-10}\left(\dfrac{E}{100\ \text{MeV}}\right)^{-2.32} exp\left(\dfrac{-E}{279\ \text{GeV}}\right), & 890\ \text{keV} < E \leqslant 200\ \text{MeV} \end{cases} \quad (3)$$

The normalization constant C, truncation energy E_b, and power-law indices α_1 and α_2 are denoted in the equation. The values are $C = (10.15 \pm 0.8) \times 10^{-2}$, $E_b = 29.99 \pm 1.1$ keV, $\alpha_1 = 1.32 \pm 0.018$, and $\alpha_2 = 2.88 \pm 0.015$. For CXB, the energy interval in our simulation is 1 keV to 100 GeV, covering the HXI detection energy range.

2.2.3. Secondary Particles

Secondary particles are generated through the interaction of primary particles with atmospheric molecules. The fluxes of these secondary particles are influenced by the geomagnetic field as they are dependent on the primary particles. Previous simulations have shown that the secondary particles background on HXI is primarily caused by albedo photons (Liu et al. 2022).

The vertical spectrum of an albedo photon at the geomagnetic cutoff rigidity $R_{\rm cutoff} \approx 4.5$ can be represented as a three-piece power-law fit (Mizuno et al. 2004; Abdo et al. 2009).

$$\frac{dI(E)}{dE}(\text{photons m}^{-2}\,\text{s}^{-1}\,\text{sr}^{-1}\,\text{MeV}^{-1}) = \begin{cases} -1010\left(\frac{E}{\text{MeV}}\right)^{-1.34}, & E \leqslant 20\text{MeV} \\ 7290\left(\frac{E}{\text{MeV}}\right)^{-2.0}, & 20\text{MeV} < E \leqslant 200\text{MeV} \\ 0.1823\left(\frac{E}{200\text{MeV}}\right)^{-2.8}, & E > 200\text{MeV} \end{cases} \quad (4)$$

The albedo photon flux relationship varies with geomagnetic cutoff rigidity, where $\frac{dI(E)}{dE} \propto R_{\rm cutoff}^{-1.13}$ for $R_{\rm cutoff} \geqslant 3$ (Thompson et al. 1981). For magnetic latitudes where $R_{\rm cutoff} < 3$ (indicating $\theta_M > 45°$), the $R_{\rm cutoff}$ was set to the minimum value of 3 for the equation. The energy range under consideration spans from 1 keV to 100 GeV.

2.2.4. South Atlantic Anomaly (SAA)

The SAA is characterized by a high proton flux. When ASO-S traverses this region, the HXI ceases operation to protect the equipment, yet the high-energy protons activate the satellite materials. During this activation process, the high-energy protons interact with the atomic nuclei of the materials, resulting in the production of radioactive isotopes. These isotopes subsequently decay, generating secondary particles. Consequently, the generation cycle of these secondary particles is determined by the half-lives of the relevant radioactive isotopes. Even after the satellite has passed through the SAA, the activated elements will continue to contribute to the delayed background. Figure 5 illustrates the average energy spectrum of protons within the SAA region along the ASO-S orbit, while Figure 6 depicts the satellite's traversal through the SAA region over the course of a single day. In our simulation, the AP-8 model available on the SPENVIS website is used to obtain the proton flux and other relevant statistics within the SAA, with the energy range of trapped protons set from 10 to 400 MeV.

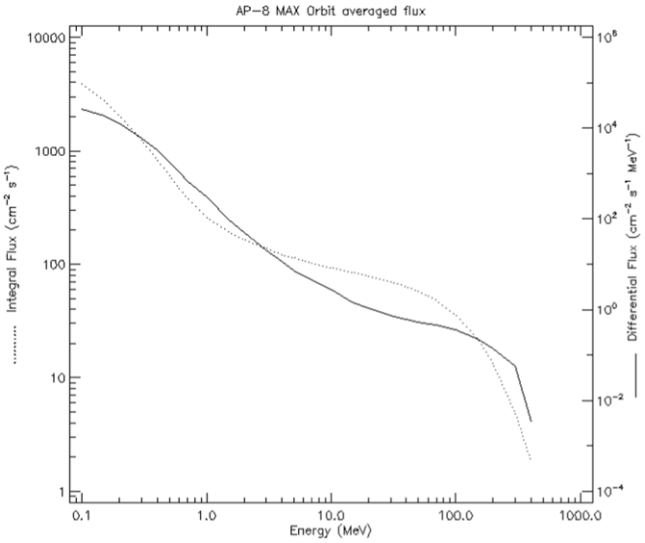

Figure 5. The averaged trapped electrons' energy spectrum for the orbit of ASO-S. The data is sourced from the SPENVIS website.

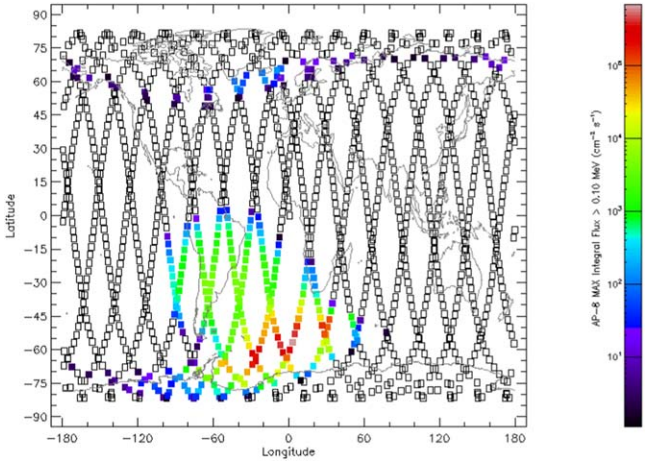

Figure 6. World map of the trapped proton flux above 0.1 MeV for the orbit of ASO-S. The data is sourced from the SPENVIS website.

2.3. Physics Processes

The activation of satellites can be triggered by high energy protons. Because of this, the radioactive decay process needs to be integrated into the physics list. Since the energy range of significance for the Hard X-ray Imager (HXI) spans from 30 to 200 keV, we opted for the QGSP_BIC_HP_LIV Physics List in our simulation model. As detailed in Liu et al. (2022), we incorporated the G4RadioactiveDecay process and established a cutoff length of 10 μm.

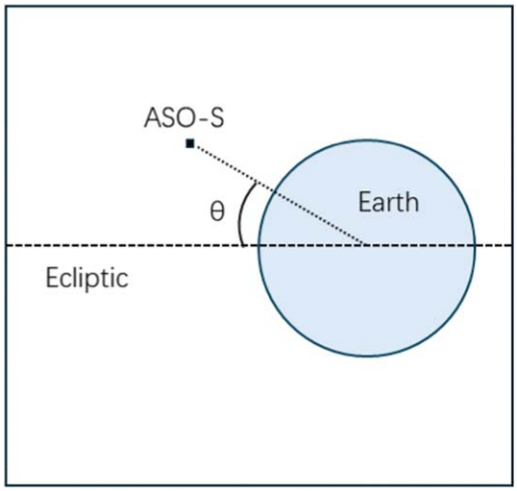

Figure 7. The position of a satellite relative to Earth can be described by the angle θ, which can be simplified as the angle between the satellite and the ecliptic plane. In this figure, sunlight is assumed to be perpendicular to the plane of representation, directed outward from the page.

3. Simulation and Observation

The detector's background is determined by the satellite's position. Specifically, the geomagnetic latitude determines the geomagnetic cutoff rigidity, which in turn influences the flux and energy spectrum of background particles; the Earth's shadowing effect is contingent upon the positional relationship between the satellite and the Earth. The positional relationship between the detector and the Earth can be described by the angle θ. Given that the satellite operates on a Sun-synchronous orbit along the terminator, its orientation is nearly perpendicular to the ecliptic plane, allowing θ to be approximated as the angle between the satellite and the ecliptic plane, as illustrated in Figure 7. The in-orbit data that we selected is from 2023 June, close to the summer solstice. At this time, the ecliptic plane and the equatorial plane intersect along the terminator. The angle between the satellite and the equatorial plane (i.e., the latitude) can be considered as the projection of the angle between the satellite and the ecliptic plane. Therefore, θ can be calculated from the satellite's latitude, as shown in Figure 8.

Geomagnetic latitude can be derived through geomagnetic models, using the satellite's longitude, latitude, and altitude. The geomagnetic model that we employ is WMM 2020, which is applicable for geomagnetic calculations from 2020 to 2025. Both geomagnetic latitude θ_m, and θ are related to latitude, but they do not correspond one-to-one with each other; within a certain range, they can be freely assigned values. In this study, we have chosen to set θ equal to θ_m. When processing in-orbit data, we also select data from positions where these values are approximately equal. To analyze the background at different geomagnetic latitudes, we planned to uniformly select four geomagnetic latitudes from the magnetic equator to the magnetic pole (i.e., 0°, 30°, 60°, 90°). However, considering that 90° corresponds to only one point at the magnetic pole, resulting in very limited in-orbit data, we replaced it with 80°. Consequently, we have chosen the geomagnetic latitudes of 0°, 30°, 60°, and 80°.

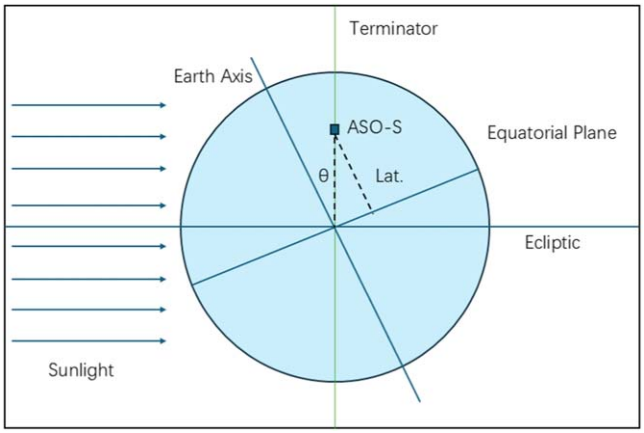

Figure 8. At the summer solstice, the ecliptic plane and the equatorial plane intersect along the terminator. At this juncture, the angle θ between the satellite and the ecliptic plane can be calculated from the latitude.

3.1. Simulation Output

Sensitive detectors in the ASO-S mass model are defined for lanthanum bromide ($LaBr_3$) of HXI. These detectors record critical information such as deposited energy and response time. The collected data is categorized into prompt and delayed (or radioactive) backgrounds based on the detector's response time following an incident. Prompt backgrounds cause immediate activation of the sensitive detector upon incident occurrence. Conversely, radioactive backgrounds can trigger signals on the sensitive detector hours, days, or even months to years after the initial incident. To quantify these radioactive backgrounds, the deposited energy and corresponding response time are initially recorded through Geant4 simulation. Subsequently, these parameters are integrated over the radiation history to determine the final background level.

The diagram in Figure 2 (right) depicts the final simulation output as an 11 × 9 matrix, detailing the counts of selected particle types within specific energy ranges of each detector. Additionally, the positions of other components of ASO-S are indicated within this visual representation.

3.2. Simulation of Charged Particles

Figure 9 illustrates the background distribution of primary protons at a geomagnetic latitude of $\theta_M = 0°$. A clear distinction is observable between the distributions of low- and high-energy particles. Low-energy measurements predominantly cluster near the detectors adjacent to the satellite's platform, likely originating from low-energy secondary particles generated by high-energy particle interactions with the

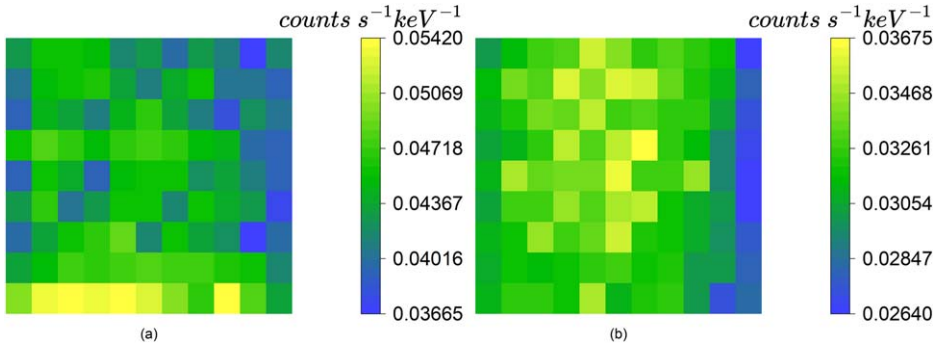

Figure 9. Simulated detector's response to primary proton at geomagnetic latitude $\theta_M = 0°$. (a) The count rate of particles in the energy range of 20–100 keV, with a maximum value of 0.05420 counts s^{-1} keV^{-1}; (b) The count rate of particles in the energy range of 100–300 keV, with a maximum value of 0.03675 counts s^{-1} keV^{-1}.

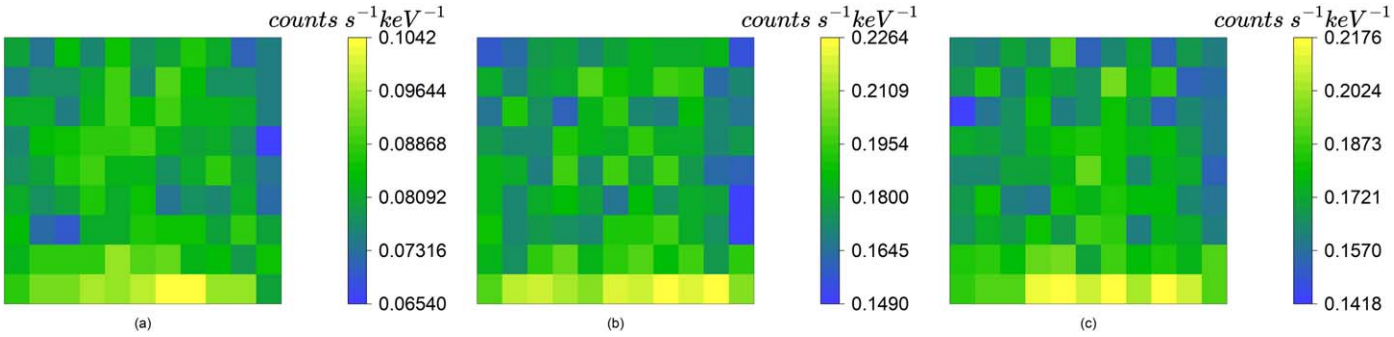

Figure 10. Simulated detector response of primary proton at various geomagnetic latitudes in the energy range of 20–100 keV. (a) The count rate at a geomagnetic latitude of $\theta_M = 30°$, with a maximum value of 0.1042 counts s^{-1} keV^{-1}; (b) The count rate at a geomagnetic latitude of $\theta_M = 60°$, with a maximum value of 0.2264 counts s^{-1} keV^{-1}; (c) The count rate at a geomagnetic latitude of $\theta_M = 80°$, with a maximum value of 0.2176 counts s^{-1} keV^{-1}.

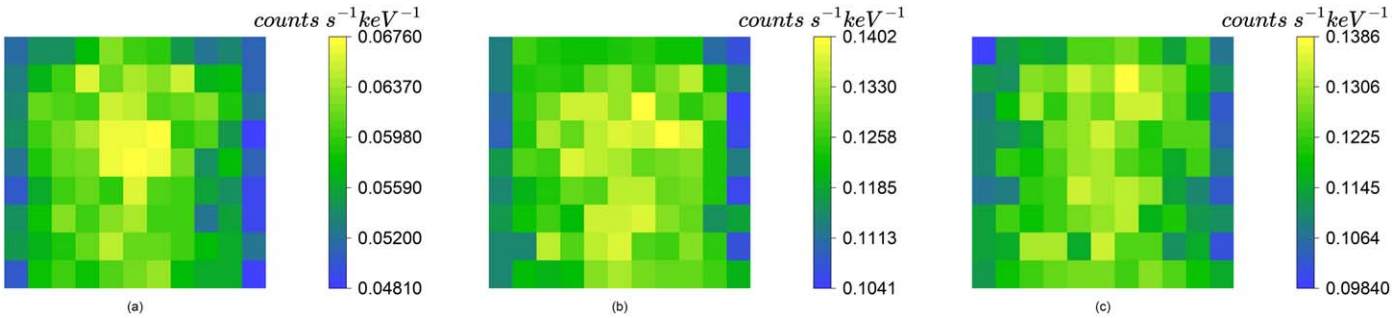

Figure 11. Simulated detector response of primary proton at various geomagnetic latitudes in the energy range of 100–300 keV. (a) The count rate at a geomagnetic latitude of $\theta_M = 30°$, with a maximum value of 0.06760 counts s^{-1} keV^{-1}; (b) The count rate at a geomagnetic latitude of $\theta_M = 60°$, with a maximum value of 0.1402 counts s^{-1} keV^{-1}; (c) The count rate at a geomagnetic latitude of $\theta_M = 80°$, with a maximum value of 0.1386 counts s^{-1} keV^{-1}.

platform. Conversely, high-energy measurements concentrate at the detector's center, possibly resulting from particle showers initiated by high-energy particles within the detector. These showers are cascade reactions that produce multiple secondary particles as they propagate through the detector. On the Earth-facing side, energetic particles encounter a barrier that impedes their entry into the detector, resulting in lower counts on the opposite side.

Figures 10 and 11 illustrate the variation in primary proton background at different geomagnetic latitudes. The background distribution exhibits distinct patterns across various geomagnetic latitudes due to the changing positions of Earth's occlusion. As

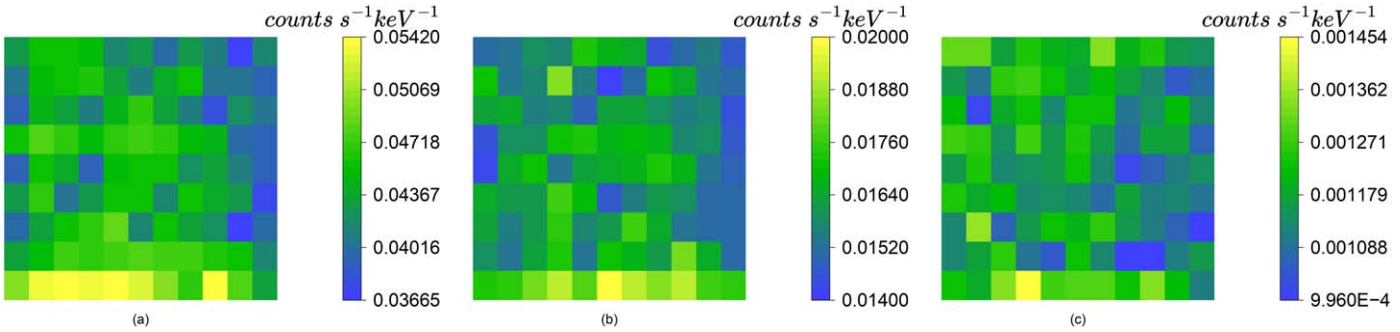

Figure 12. The simulated detector's response in the energy range of 20–100 keV to different types of primary charged particles at geomagnetic latitude $\theta_M = 0°$. (a) The count rate attributed to protons, with a maximum value of 0.05420 counts s^{-1} keV^{-1}; (b) The count rate attributed to alpha particles, with a maximum value of 0.02000 counts s^{-1} keV^{-1}; (c) The count rate attributed to electrons, with a maximum value of 0.001454 counts s^{-1} keV^{-1}.

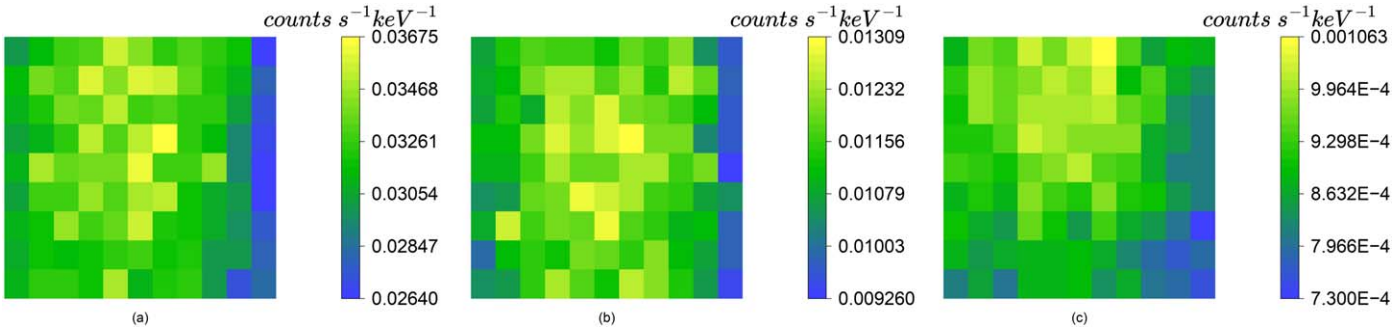

Figure 13. The simulated detector's response in the energy range of 100–300 keV to different types of primary charged particles at geomagnetic latitude $\theta_M = 0°$. (a) The count rate attributed to protons, with a maximum value of 0.03675 counts s^{-1} keV^{-1}; (b) The count rate attributed to alpha particles, with a maximum value of 0.01309 counts s^{-1} keV^{-1}; (c) The count rate attributed to electrons, with a maximum value of 0.001063 counts s^{-1} keV^{-1}.

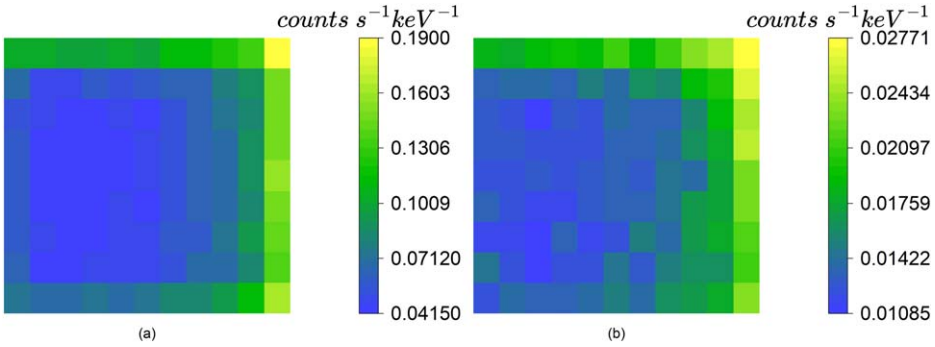

Figure 14. Simulated detector response of CXB at geomagnetic latitude 0°. (a) The count rate of particles in the energy range of 20–100 keV, with a maximum value of 0.1900 counts s^{-1} keV^{-1}; (b) The count rate of particles in the energy range of 100–300 keV, with a maximum value of 0.02771 counts s^{-1} keV^{-1}.

geomagnetic latitude increases, there is a corresponding rise in primary proton flux, leading to an increase in the background counts they generate. However, at a geomagnetic latitude of 80°, an anomalous decrease in counts is observed. This decline can be attributed to the fact that the primary proton background predominantly originates from secondary particles generated through interactions with satellite components. With increasing latitude, Earth gradually obstructs the satellite platforms, resulting in a reduction of secondary particle production, which counteracts the increase in primary proton flux.

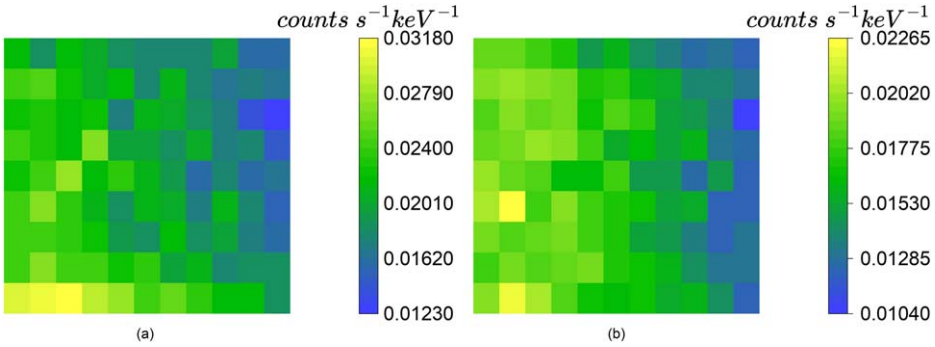

Figure 15. Simulated detector response of albedo photon at geomagnetic latitude 0°. (a) The count rate of particles in the energy range of 20–100 keV, with a maximum value of 0.03180 counts s^{-1} keV^{-1}; (b) The count rate of particles in the energy range of 100–300 keV, with a maximum value of 0.02265 counts s^{-1} keV^{-1}.

Table 3
Under the Average Flux Per Second, the Delayed Background Count Rates Generated by the Detectors' Responses to the SAA and Primary Protons ($\theta_M = 0°$) During different Time Periods

	Instant (<1 ms)	S	Minute	Hr	Day	Month	Yr	1 Yr Later
SAA	110999	18	47	106	98	68	20	124
primary proton	983.251	0.034	0.281	0.519	0.426	0.247	0.060	0.426

As illustrated in Figures 12 and 13, the background count distributions of protons, alpha particles, and electrons on the detector exhibit remarkably similar patterns, despite their varying absolute counts. Table 4 documents the count rates of the detectors' responses to primary charged particles at various geomagnetic latitudes, as derived from simulation.

3.3. Simulation of Photons

Photons in the background radiation originate from two primary sources: the Cosmic X-ray Background (CXB) and Earth's albedo. Table 4 presents the count rates of the background signals produced by photons on the detectors, as obtained through simulation.

Figures 14 and 15 illustrate the count distribution of CXB and albedo photons, respectively, at geomagnetic latitude $\theta_M = 0°$. The count distribution is primarily influenced by the relative positions of the detector and Earth. For CXB, fewer counts are observed on the Earth-facing side due to Earth's occlusion, while the side opposite Earth shows higher counts due to reduced occlusion. Conversely, for albedo photons, this pattern is reversed. Notably, unlike charged particles, the count distribution across different energy ranges remains relatively consistent for both CXB and albedo photons.

The energy spectrum and flux of CXB are position-independent, resulting in similar CXB backgrounds across various latitudes, with minor variations attributable to Earth's occlusion effects, as demonstrated in Figure 16. Albedo photons, being secondary particles, inherit their flux and energy spectrum from the primary particles that generate them. This inheritance leads to an increase in counts with geomagnetic latitude, as illustrated in Figure 17.

3.4. Simulation of Delay Background

The materials on the satellite are activated by high-energy protons, producing radioactive isotopes. The particles generated by the decay of these radioactive isotopes, if they enter the $LaBr_3$ crystal, will produce a delayed background on the detector. The time at which the delayed background is generated is related to the half-life of the radioactive elements produced by activation.

Figure 18 shows the variation of background generated by protons in the SAA region and primary protons over time. As shown in the figure, there is almost no background generated between 1 ms and 1 s, which can be used as the boundary between instantaneous background and delayed background. That is, the background generated within 1 ms is considered as instantaneous background, while the background generated after that is regarded as delayed background. Table 3 shows the background counts in different time periods.

It can be seen that the vast majority (approximately 99.8%) of the background counts are contributed by the instantaneous background. Therefore, the delayed background from primary protons is usually not necessary to consider. However, due to the extremely high flux of high-energy protons in the SAA

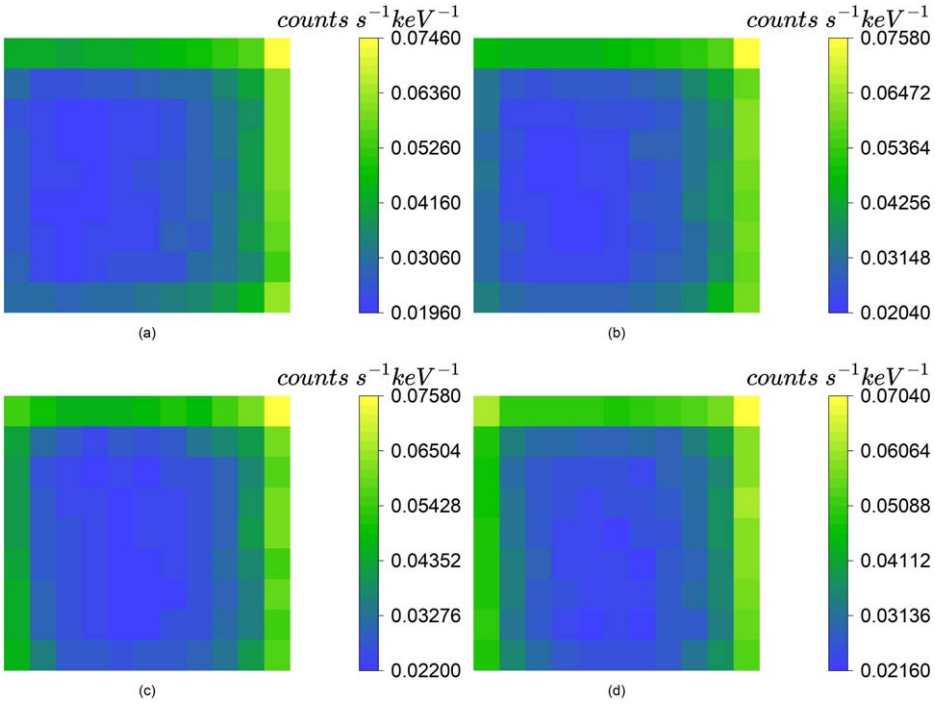

Figure 16. Simulated detector response of CXB at different geomagnetic latitudes. (a) The count rate at geomagnetic latitude 0°, with a maximum value of 0.07460 counts s^{-1} keV^{-1}; (b) The count rate at geomagnetic latitude 30°, with a maximum value of 0.07580 counts s^{-1} keV^{-1}; (c) The count rate at geomagnetic latitude 60°, with a maximum value of 0.07580 counts s^{-1} keV^{-1};(d) The count rate at geomagnetic latitude 80°, with a maximum value of 0.07040 counts s^{-1} keV^{-1}.

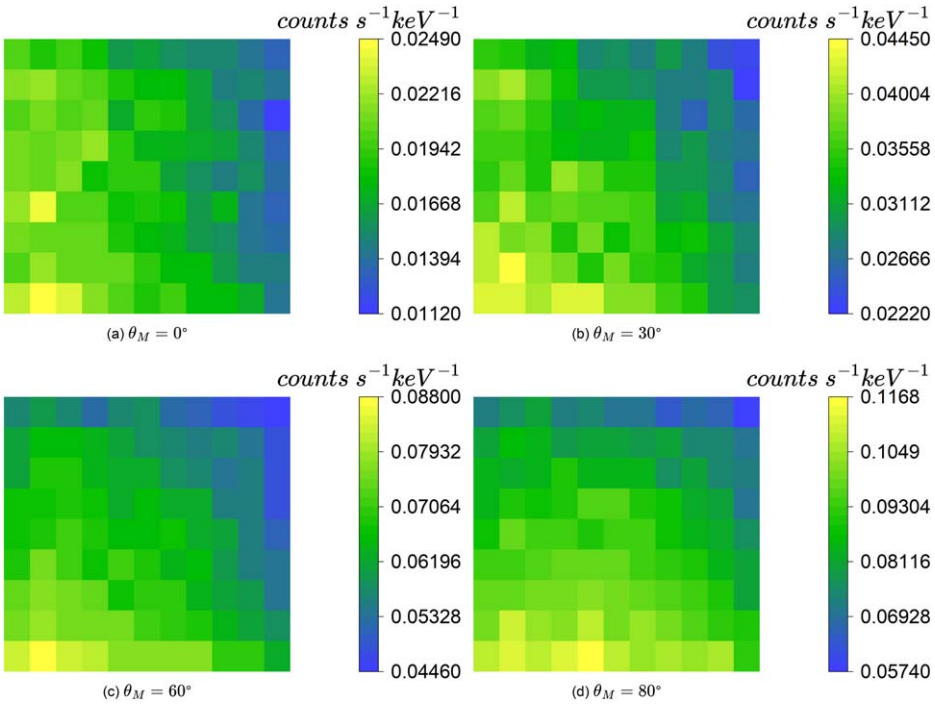

Figure 17. Simulated detector response of albedo photon at different geomagnetic latitudes. (a) The count rate at geomagnetic latitude 0°, with a maximum value of 0.02490 counts s^{-1} keV^{-1}; (b) The count rate at geomagnetic latitude 30°, with a maximum value of 0.04450 counts s^{-1} keV^{-1}; (c) The count rate at geomagnetic latitude 60°, with a maximum value of 0.08800 counts s^{-1} keV^{-1}; (d) The count rate at geomagnetic latitude 80°, with a maximum value of 0.1168 counts s^{-1} keV^{-1}.

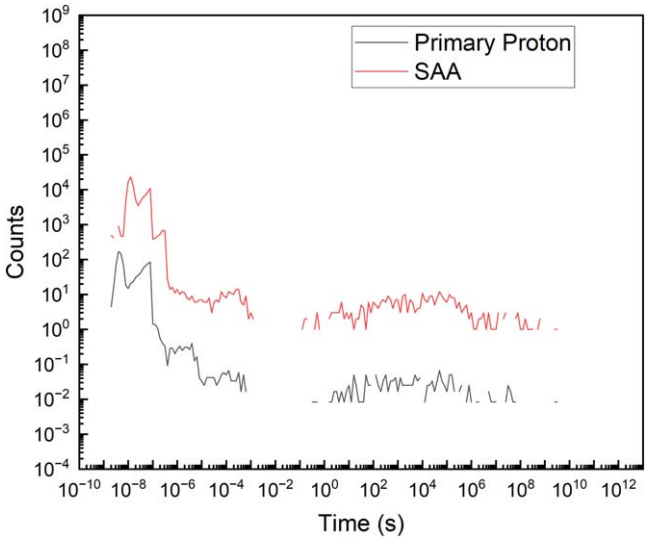

Figure 18. The temporal variation of the detectors' responses to the SAA and primary protons ($\theta_M = 0°$) under the average flux per second.

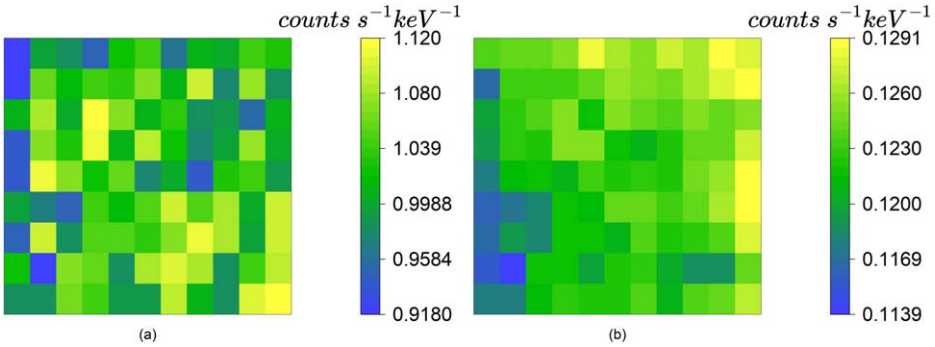

Figure 19. Internal background from ground testing, including embedded radiation sources and lanthanum-138. (a) The count rate of particles in the energy range of 20–100 keV, with a maximum value of 1.120 counts s^{-1} keV^{-1}; (b) The count rate of particles in the energy range of 100–300 keV, with a maximum value of 0.1291 counts s^{-1} keV^{-1}.

region, the delayed background generated will still contribute to the total background count rate.

3.5. In-orbit Observation

During orbital operation, the detector background comprises two main components. In addition to the background from external space particles that we have simulated, there are internal background signals generated within the detector itself. Integrated radiation sources in the detector produce counts significantly higher than the space background to meet energy calibration requirements. Furthermore, the decay of La-138, a radioactive isotope presented in the lanthanum bromide crystals within the detector, contributes to the background signal. These internal backgrounds were evaluated through ground experiments conducted before the satellite's launch, with the results illustrated in Figure 19. The total count rate recorded during the ground test was 11291.247 s^{-1}, with an average count rate per detector of 114.053 s^{-1} $detector^{-1}$.

The data utilized in this study are derived from observations made in 2023 May and June, with geomagnetic latitudes determined based on the satellite's positional data. To obtain specific geomagnetic latitude observational data, anomalous events such as solar flares and radiation belt entries were excluded from the in-orbit data analysis.

3.6. Conclusion

The simulation results presented in Table 4 demonstrate that primary protons constitute the majority of background counts across all modeled sources, contributing nearly half of the total counts. Photons follow, with counts from the CXB being higher than those from albedo photons at low geomagnetic latitudes. However, as the geomagnetic latitude increases, the counts from CXB change very little, while the counts from

Table 4
The Contribution of Different Source to the Simulated Detector Response (count rate) at Different Geomagnetic Latitudes (energy range: 20–300 keV)

Source	Counts of all Detector (s^{-1})			
	$\theta_M = 0°$	$\theta_M = 30°$	$\theta_M = 60°$	$\theta_M = 80°$
primary proton	985.242 ± 2.865	1818.650 ± 5.506	3936.070 ± 11.454	3783.320 ± 12.301
primary alpha	356.123 ± 1.090	572.247 ± 1.953	932.725 ± 4.829	886.500 ± 3.843
primary electron	27.225 ± 0.082	67.305 ± 0.183	408.647 ± 1.167	461.620 ± 1.359
CXB	890.110 ± 2.983	917.280 ± 3.039	957.780 ± 3.095	977.610 ± 3.127
Albedo gamma-ray	501.060 ± 2.238	927.380 ± 4.306	1784.180 ± 5.973	1999.226 ± 6.323
Total	2759.760 ± 4.829	4302.862 ± 7.866	8019.402 ± 14.182	8108.276 ± 14.755
Average Count per Detector	27.876 ± 0.049	43.463 ± 0.079	81.004 ± 0.143	81.902 ± 0.149

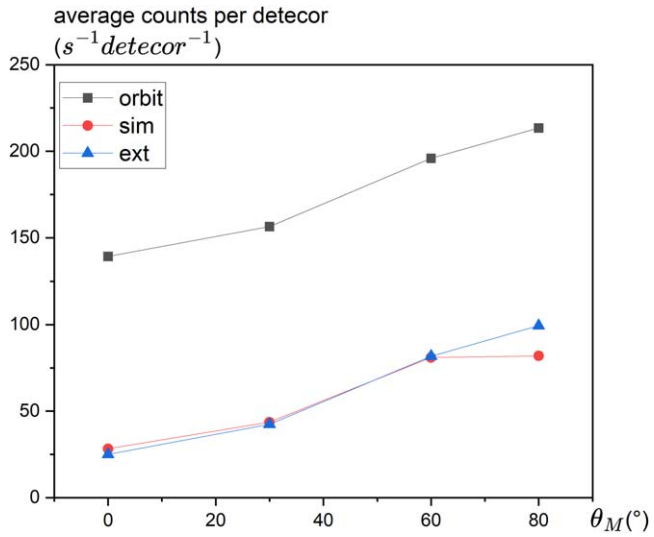

Figure 20. Comparison of in-orbit data with simulation data. "orbit": the count rate obtained from in-orbit observations; "sim": the detector response of our simulation; "ext": the in-orbit external background count rate, which was calculated by subtracting the internal background (measured on the ground) from the total background observed in orbit.

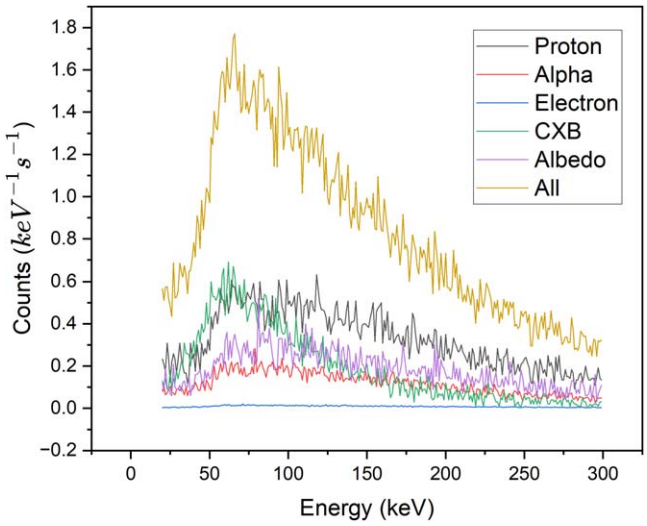

Figure 21. The background energy spectrum of the detector unit D33, simulated at a geomagnetic latitude of 0°.

albedo photons rise rapidly. Therefore, in high geomagnetic latitude regions, albedo photons become dominant. The behavior of charged particles within primary cosmic rays is modulated by geomagnetism, resulting in varying detector counts based on geomagnetic latitude. As geomagnetic latitude increases, background counts from charged particles also increase. Notably, electrons, due to their lower charge-to-mass ratio, are more susceptible to magnetic field effects. Among primary cosmic ray particles at the same geomagnetic latitude, protons yield the highest background counts, followed by alpha particles, with electrons producing the lowest counts.

After collecting orbital data and utilizing ground test data to eliminate internal background, we compared the results with simulation data, as illustrated in Figure 20. The comparison reveals close agreement at geomagnetic latitudes (θ_M) of 0°, 30°, and 60°. However, a notable discrepancy emerges in the in-orbit background at $\theta_M = 80°$, where observed values exceed simulation predictions. This variance may be attributed to limitations in the albedo photon spectrum model for cases where the geomagnetic cutoff rigidity ($R_{\rm cutoff}$) exceeds 3. At $\theta_M = 80°$, where $R_{\rm cutoff} \ll 3$, the simulated spectrum may deviate from actual observations. Given that backgrounds from other particle simulations align with in-orbit observations, our observational data presents an opportunity for future research to investigate the spectral distribution and flux of albedo photons in this regime.

By comparing the simulated background with the in-orbit observed energy spectrum, further information can be obtained. Here, one of the detector units is selected for demonstration. Figure 21 illustrates the background energy spectrum obtained through simulation for the detector unit located in the 4th row and 3rd column of Figure 2 (labeled as D33). Subsequently, it is compared with the energy spectrum acquired from in-orbit observations of the same detector unit, with the results displayed in Figure 22. It can be observed that the in-orbit

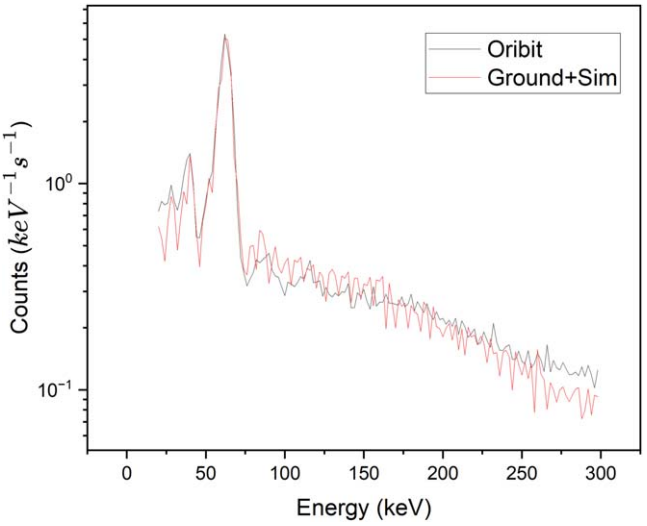

Figure 22. The background energy spectrum of the detector unit D33 at a geomagnetic latitude of 0°, juxtaposing observational data with simulated data.

and simulated energy spectra match well. Consistent results are also obtained for other detector units.

4. Summary

The HXI is one of the payloads aboard the ASO-S satellite, which operates in a Sun-synchronous orbit at an average altitude of 720 km. Analysis of this orbital environment enables the identification of particles contributing to the spatial background, as well as the determination of their spectra and spatial distribution.

This study simulates the background environment of the HXI instrument on the ASO-S satellite during its orbital trajectory. The research aims to quantify particle counts and characterize distributions from various sources detected by the instrument. Simulations conducted at low and moderate geomagnetic latitudes ($0 \leqslant \theta_M \leqslant 60°$) demonstrate strong concordance with in-orbit data, facilitating background deduction. However, discrepancies emerge at high geomagnetic latitudes ($\theta_M = 80°$), attributed to the absence of a specific model for the energy spectrum of albedo photons at $R < 3$. Despite certain simplifications in the environmental particle distribution model, the simulation demonstrates that these approximations have minimal impact on the average particle counts and background fluctuations.

Acknowledgments

This work is supported by the National Natural Science Foundation of China (NSFC, grant Nos. 12173100, 11973097 and 12022302), the Youth Innovation Promotion Association CAS (Nos. 2021317 and Y2021087) the Scientific Instrument Developing Project of the CAS (No. 20200077) and the Strategic Priority Research Program on Space Science, Chinese Academy of Sciences (No. XDA 15 320 104).

ORCID iDs

Hao-Xiang Wang https://orcid.org/0009-0003-7568-6799
Zhe Zhang https://orcid.org/0000-0003-0788-5430
Wei Liu https://orcid.org/0000-0002-1490-5172
Yang Su https://orcid.org/0000-0002-4241-9921

References

Abdo, A. A., Ackermann, M., Ajello, M., et al. 2009, PhRvD, 80, 122004
Agostinelli, S., Allison, J., Amako, K., et al. 2003, NIMPA, 506, 250
Ajello, M., Greiner, J., Sato, G., et al. 2008, ApJ, 689, 666
Alcaraz, J., Alpat, B., Ambrosi, G., et al. 2000a, PhLB, 494, 193
Alcaraz, J., Alpat, B., Ambrosi, G., et al. 2000b, PhLB, 484, 10
Alcaraz, J., Alvisi, D., Alpat, B., et al. 2000c, PhLB, 472, 215
Allison, J., Amako, K., Apostolakis, J., et al. 2006, ITNS, 53, 270
Allison, J., Amako, K., Apostolakis, J., et al. 2016, NIMPA, 835, 186
Atwood, W. B., Abdo, A. A., Ackermann, M., et al. 2009, ApJ, 697, 1071
Campana, R., Feroci, M., Del Monte, E., et al. 2013, ExA, 36, 451
Churazov, E., Sunyaev, R., Revnivtsev, M., et al. 2007, A&A, 467, 529
Fukazawa, Y., Mizuno, T., Watanabe, S., et al. 2009, PASJ, 61, S17
Gan, W.-Q., Zhu, C., Deng, Y.-Y., et al. 2019, RAA, 19, 156
Gendreau, K. C., Mushotzky, R., Fabian, A. C., et al. 1995, PASJ, 47, L5
Jahoda, K., Markwardt, C. B., Radeva, Y., et al. 2006, ApJS, 163, 401
Kosugi, T., Makishima, K., Murakami, T., et al. 1991, SoPh, 136, 17
Liu, W., Chen, D.-Y., Jiang, X.-K., et al. 2022, RAA, 22, 095011
Mizuno, T., Kamae, T., Godfrey, G., et al. 2004, ApJ, 614, 1113
Poole, C. M., Cornelius, I., Trapp, J. V., & Langton, C. M. 2012, Australasian Phys. & Eng. Sci. Med., 35, 329
Rothschild, R. E., Blanco, P. R., Gruber, D. E., et al. 1998, ApJ, 496, 538
Tawa, N., Hayashida, K., Nagai, M., et al. 2008, PASJ, 60, S11
Tenzer, C., Warth, G., Kendziorra, E., & Santangelo, A. 2010, Proc. SPIE, 7742, 77420Y
Thompson, D. J., Simpson, G. A., & Özel, M. E. 1981, JGR, 86, 1265
Watanabe, K., Hartmann, D. H., Leising, M. D., & The, L. 1999, ApJ, 516, 285
Xiao, J., Qi, L., Zhang, S.-N., et al. 2023, ExA, 56, 477
Xie, F., & Pearce, M. 2018, Galax, 6, 50
Zhang, Z., Chen, D.-Y., Wu, J., et al. 2019, RAA, 19, 160
Zombeck, M. V. 2006, Handbook of Space Astronomy and Astrophysics (3rd ed.; Cambridge: Cambridge Univ. Press)